ACS EARTH AND SPACE CHEMISTRY

http://pubs.acs.org/journal/aesccq

Article

Inhibition of Chromium(III) Oxidation through Manganese(IV) Oxide Passivation and Iron(II) Abiotic Reduction

Miranda L. Aiken, Macon J. Abernathy, Michael V. Schaefer, Ilkeun Lee, and Samantha C. Ying*

Cite This: *ACS Earth Space Chem.* 2023, 7, 2327−2338

Read Online

ACCESS | Metrics & More | Article Recommendations | Supporting Information

ABSTRACT: Manganese (Mn) oxides are strong oxidants that are ubiquitous in soils and can oxidize redox-active metals, including chromium (Cr). In soil environments, trivalent chromium (Cr(III)) is a benign, immobile micronutrient, whereas the hexavalent Cr(VI) form is present as a highly mobile, toxic chromate oxyanion. Although many studies have characterized the capacity of Mn(III/IV) oxides to oxidize Cr(III) to toxic Cr(VI), the oxidative capacity of Mn oxides in the presence of potentially passivating soil constituents, specifically reduced soluble iron ($Fe(II)_{aq}$), remains unresolved. We hypothesized that chemical processes at redox interfaces, such as diffusion-limited environments within soil aggregates, can lead to decreased Cr(VI) production from Mn oxide-driven oxidation due to passivation by $Fe(II)_{aq}$. A multichamber diffusion-limited reactor was used to simulate transport at soil redox interfaces and investigate the capacity of poorly crystalline and crystalline Mn oxides to oxidize solid Cr(III) minerals to Cr(VI) in the presence of $Fe(II)_{aq}$. As predicted, Cr(VI) was produced through the Mn oxide-catalyzed oxidation of Cr(III) at a rate controlled by the solubility of $Cr(OH)_3$. However, in the presence of $Fe(II)_{aq}$, the concentration of aqueous Cr(VI) decreased as a function of the $Fe(II)_{aq}$ concentration, where high concentrations of $Fe(II)_{aq}$ completely inhibited Cr(VI) production, likely through both the passivation of the Mn oxide and the direct reduction of Cr(VI) by Fe(II). At both low (14 μM) and high (100 μM) $Fe(II)_{aq}$ concentrations, the iron oxide minerals hematite (Fe_2O_3) and goethite (α-FeOOH) were associated with the Mn oxides, which can cause surface passivation, a likely role that decreases Cr(III) oxidation. Additionally, the Cr(III) oxidation rate decreased with increasing crystallinity of the Mn oxides whether or not Fe(II) was present.

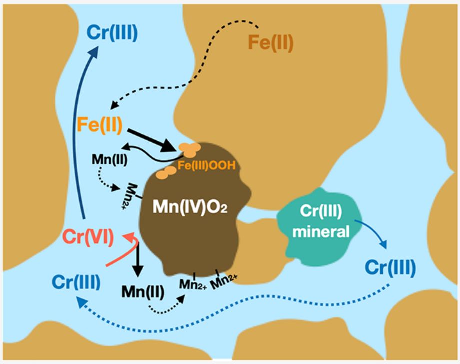

KEYWORDS: *hexavalent chromium, Cr(VI), birnessite, pyrolusite, contamination, aggregates, diffusion*

1. INTRODUCTION

Chromium is a naturally occurring and anthropogenically sourced redox-active soil and water contaminant that predominantly occurs in the Cr(III) and Cr(VI) oxidation states.[1−3] Cr(III) is an essential trace micronutrient, whereas the ingestion of Cr(VI) can lead to adverse human health outcomes, including cancer.[4] In soils and sediments, trivalent chromium is commonly found as a sparingly soluble hydroxide precipitate that can form strong mineral complexes,[5] while hexavalent chromium is present as a highly mobile, toxic chromate oxyanion in groundwater sources.[6,7] Chromite, Cr−magnetite, and Cr-bearing silicates are common sources of geogenic Cr(III) in soils and sediments, which can undergo in situ abiotic oxidation to Cr(VI).[8] Because Cr(III)-bearing minerals cover roughly 1% of the earth's surface, concentrated along plate boundaries, understanding the processes that enhance or inhibit the abiotic oxidation of Cr(III) to Cr(VI) has implications for global groundwater quality and those who rely on it.[7,8]

Prior to oxidation, the dissolution of Cr(III) from Cr-bearing minerals and the migration of Cr(III) to Mn oxide solids must occur. In well-mixed environments, Cr(III) oxidation is limited by the solubility of the Cr(III) mineral and the distance it must travel to the site of oxidation.[9−11] Increasing Fe substitution in $Cr_xFe_{1-x}(OH)_3$ secondary minerals decreases the solubility of the mineral, thus decreasing Cr(VI) generation.[9,11]

While Mn(II)-oxidizing bacteria has been observed to oxidize Cr(III),[12] the abiotic oxidation of Cr(III) in soils is dominantly catalyzed by Mn(III/IV) oxides.[6,13,14] Mn(III/IV) oxides in soils are generally biogenic, poorly crystalline, layered, mixed-valence Mn(III/IV) minerals resembling birnessite. In contrast, pyrolusite is a crystalline, tunnel-structured (1 × 1 octahedra), single-valence Mn(IV) mineral.[15−17] While pyrolusite is less commonly found in soil environments, reactions with pyrolusite can serve as an end-member case for Mn(IV)-driven oxidation.[18] Because of the

Special Issue: Environmental Redox Processes and Contaminant and Nutrient Dynamics

Received: May 23, 2023
Revised: October 25, 2023
Accepted: October 26, 2023
Published: November 13, 2023

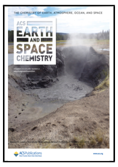

https://doi.org/10.1021/acsearthspacechem.3c00141

collective differences between the two minerals in their surface area (98−224 m^2/g for birnessite and 6−8 m^2/g for pyrolusite), mineral structure, reactive sites, stability, and valence characteristics, birnessite is more reactive than pyrolusite.[17,19,20] Under reducing conditions, anaerobic microbial respiration can produce reduced species such as Fe(II), Mn(II), and carbonate, which can decrease the oxidative capacity of Mn oxides,[21−23] therefore potentially inhibiting Mn oxide-driven Cr(VI) production. Simultaneously, Fe(II) can also directly reduce Cr(VI) to form very weakly soluble Cr(III)−Fe(III) hydroxides as a dominant abiotic mechanism of Cr immobilization under reducing conditions.[24]

Pore networks connect complex, heterogeneous soil aggregate structures within soil environments. Dissolved oxygen moves through larger pore throats via advective flow, whereas diffusive transport dominates within finer pore throats, including intra-aggregate pores.[25] Within the soil aggregate, the rate of oxygen consumption in the interior of the aggregates can be greater than the rate of oxygen supplied by diffusion, creating a redox gradient from the exterior to the interior of the aggregates.[26,27] These sustained anaerobic microsites within soil aggregates support microbial Fe(III) respiration, producing soluble Fe(II) that diffuses to the oxygenated or more oxidizing aggregate exterior.[28−30] Ying et al.[29] and Masue-Slowey et al.[28] demonstrated that the abiotic oxidation of Fe(II) with molecular oxygen and Mn oxides at the aggregate exterior leads to Fe(III) hydroxide precipitation, which can act as a high-affinity and high-capacity adsorbent for reduced metal contaminants, such as arsenic, co-transported outward from the aggregate center. Within the oxic exterior of soil aggregates, it has been demonstrated that Cr(VI) reduction occurs due to the increased organic carbon and microbial activity, which drives either direct reduction or the release of reactive reductants such as Fe(II) that then reduce Cr(VI).[30,31]

Although the aforementioned abiotic Cr oxidation and reduction pathways have been investigated individually, a systems approach better represents the soil environment, where reactive minerals can be physically separated in space, the movement of aqueous species may be limited by diffusion, and co-occurring elements may alter the oxidative potential of the system. Despite the rate limitations of geogenic Cr(VI) production in soils, Cr(VI) formation is observed in these highly structured soil environments, where it can then migrate into aquifers that are used as drinking water sources.[32,33]

In this study, we reveal how the co-occurrence of Fe(II) and Cr(III) within a diffusion-controlled environment may alter the oxidative potential of Mn oxides and, therefore, the oxidation of Cr(III) to Cr(VI). To do this, we utilize a diffusion-limited reactor to model highly structured soil environments. We also examine the effect of (1) Mn oxide crystallinity on Cr(III) oxidation, using pyrolusite and birnessite as representatives of end members, and (2) Fe(II) concentration on Cr(VI) production, using varying concentrations that are representative of those observed at the surface of constructed soil aggregates. We hypothesized that Cr(III) oxidation would occur despite diffusion limitations and that the amount of Cr(VI) that was produced would decrease as the Fe(II) concentration increased.

2. MATERIALS AND METHODS

A multichamber reactor was used to investigate the impact of high and low Fe(II) concentrations on the capacity of birnessite, a poorly crystalline, layer-structured Mn(III/IV) oxide that is commonly found in the environment, and pyrolusite, a crystalline, layer-structured Mn(IV) oxide, to oxidize Cr(III) from chromium hydroxides ($Cr(OH)_3$, moderate solubility) in a diffusion-controlled environment. Pyrolusite was chosen as a model Mn(IV) end member. The multichamber reactor has been described in detail previously. Aside from simulating transport-limited conditions, the multichamber reactor is uniquely designed to maintain the physical separation of solid phases within their respective chambers, allowing for the detailed solid-phase analysis of individual mineral phases over time, which is impossible within a homogeneous batch or synthetic aggregate reactor systems.

2.1. Mineral Synthesis. Cr(III) hydroxides ($Cr(OH)_3$) were synthesized by titrating a 50 mM solution of $CrCl_3$ to a pH of 6 with NaOH and stirring it for 24 h at room temperature, similar to the procedure described by Hansel et al.[34] The solids were centrifuged, triple-rinsed with double deionized water (DDI water, 18 MΩ cm), dried in a warm oven (30 °C), and ground before experimental use. Birnessite was synthesized following the protocol described by McKenzie.[35] First, 63 g of $KMnO_4$ (Fisher Scientific) was dissolved into 1 L of DDI water and heated to 90 °C. While vigorously stirring, 66 mL of concentrated HCl was added to the heated $KMnO_4$ solution in a 4 L flask and maintained at the same temperature for 10 min. After letting the slurry cool for 30 min, the oxides were filtered through 50 μm ashless filter paper (Whatman) and triple-washed with DDI water. The dried solids were ground with an agate mortar and pestle before experimental use. Pyrolusite was purchased from Sigma-Aldrich (ReagentPlus, ≥99%). The pyrolusite and birnessite mineralogy were confirmed with powder X-ray diffraction (XRD) (Figure S1) using a Siemens D500 diffractometer with a Cu Kα X-ray source operating at 40 kV. JADE software (Materials Data, Inc.) was used to analyze the data, and peak positions and intensities were matched with data from the RRUFF database (rruff.info). The surface area of the minerals was determined with multisurface BET (Brunauer−Emmett−Teller) and adsorption−desorption BJH (Barrett−Joyner−Halenda) methods using a Quantachrome NOVA 2000e instrument.

2.2. Multichamber Reactor. All experiments were conducted in an anoxic glovebag (95% N_2:5% H_2 atmosphere; Coy) at ambient temperature (25 °C). The multichamber diffusion reactor was constructed using polyvinyl chloride (PVC) pipes (ID 209-030, internal diameter of 7.6 cm) separated by a 0.05 μm nitrocellulose isopore filter (Millipore) to simulate diffusion-controlled transport within soil aggregates (Figure S2).

The background solution was 10 mM PIPES and 10 mM NaCl buffered at a pH of 7 to approximate the average pH and ionic strength of soil pore water, similar to previous work.[21,22,29,36−39] Manganese oxides (3.5 g) were added to 750 mL of the deoxygenated background solution in one reaction chamber and allowed to equilibrate for 24 h while being continuously stirred at 400 rpm using overhead impellers. The experiment was initiated by suspending 2 g of Cr(III) hydroxides in the adjacent reactor chamber in 750 mL of the deoxygenated buffer solution. To examine the effect of Fe(II) on Cr(VI) reduction and the inhibition of Mn oxidation, a $FeCl_2$ stock solution (3 M Fe(II)) was then added to the buffer solution in the Cr(III) hydroxide-containing chamber to obtain a final concentration of 14 μM or 100 μM in the Cr(III) hydroxide chamber. The reactions were run for 96 h and sampled throughout the experiment.

2.3. Aqueous-Phase Analysis. For aqueous analysis, 5 mL of the slurry was withdrawn from each chamber, filtered through a 0.22 μm cellulose acetate filter (CVS), and acidified with concentrated trace metal-grade HNO_3. The concentrations of Cr, Fe, and Mn were measured using inductively coupled plasma optical emission spectroscopy (ICP-OES; PerkinElmer, Optima 7300 DV). Cr(VI) was quantified following the method used by Bartlett and James[40] by using a *s*-diphenyl carbazide (DPC) colorimetric assay. The DPC reagent was made by dissolving 0.05 g of DPC in 10 mL of methanol and adding this mixture to 87.2 mL of DDI water with 2.8 mL of H_2SO_4 while minimizing light exposure. To determine Cr(VI), 0.125 mL of the DPC reagent was added to 1 mL of the filtered sample and developed for 20 min. Absorbance was measured at 540 nm on a spectrophotometer (detection limit = 0.1 μM; GENESYS 20 Thermo Spectronic).

2.4. Solid-Phase Analysis. The total concentration of solid-phase Mn, Fe, and Cr was determined by acid digestion. During sampling, 5 mL of the slurry was collected from each chamber. All liquid was evaporated from the centrifuge tubes in a 90 °C heat block. The dried solids were resuspended in 3 mL of concentrated trace metal-grade HNO_3 and agitated until dissolved. Then, the acid-dissolved samples were diluted with DDI water and analyzed using ICP-OES for Mn, Fe, and Cr. After accounting for dilutions, the final solid concentrations were calculated by subtracting the aqueous concentrations from the total digestions.

2.5. Bulk X-ray Absorption Spectroscopy. To determine the oxidation states of Cr and Mn and the mineral formation and transformation of Fe oxide over time, Mn oxide solids were collected by depositing solids from 5 mL of the slurry onto a 0.22 μm cellulose acetate filter (CVS) and drying them in an anoxic glovebag. All of the samples were stored anoxically until immediately before the X-ray analysis. The samples were transported to Stanford Synchrotron Radiation Lightsource (SSRL) in an anoxic container (Mitsubishi) with O_2 scavenging AnaeroPacks (Mitsubishi). Prior to analysis, the solids that were deposited onto the filter were sealed in 0.5 mil Kapton tape and mounted onto an aluminum sample holder.

X-ray absorption spectroscopy (XAS) spectra were collected at SSRL beamlines 4-1, 4-3, and 11-2. Mn K-edge X-ray absorption near edge structure (XANES) spectra were collected at beamline 4-1 under a liquid N_2 cryostat (~77 K) to limit Mn photoreduction. Fluorescence data were collected using a passivated implanted planar silicon (PIPS) detector with soller slits and a Cr filter (3 absorption lengths) placed 7.5 cm perpendicular to the beam path. Spectra were collected in 5 eV steps below the edge (6310−6520 eV), in 0.25 eV steps at the edge (6520−6570 eV), and in steps equivalent to 0.05 $Å^{-1}$ above the edge.

Bulk Fe K-edge extended X-ray absorption fine structure (EXAFS) spectra were collected at beamline 11-2 at room temperature using a He purge box (<0.15% O_2). Fluorescence and transmission data were collected using a 7-channel silicon drift detector or a 100-element Ge detector. Iron spectra were collected from 6922 to 7712 eV, approximately to a $k = 12$. Different points on each Fe sample were selected for the replicate scans (~5 scans) to prevent photo-oxidation. A comparison of the scans showed no indication of beam damage. Data processing and linear combination analysis (LCA) were performed using the Athena software.[41] The pre- and post-edge regions were fit with linear and third-order polynomial functions, respectively, and the spectra were normalized to an edge step of 1. Goethite, ferrihydrite, hematite, magnetite, and lepidocrocite standards were used for the LCA fitting. Cr K-edge XANES spectroscopic analysis was attempted on beamline 11-2 using a 100-element Ge detector, but because the bulk concentrations were below the detection limit, the samples were instead analyzed using micro X-ray fluorescence (μ-XRF) mapping to perform μ-XANES on Cr hotspots (details are given in section 2.6).

The average oxidation state (AOS) of manganese and the proportion of Mn(II), Mn(III), and Mn(IV) were estimated by fitting the sample spectra with a linear combination of Mn XANES reference standards ($MnSO_4$, manganite, and birnessite, respectively) following the standards library compiled by and analysis procedure outlined by Manceau.[42]

2.6. μ-XRF Imaging and Sample Preparation. The spatial distribution (namely, co-location) of Cr and Fe on the Mn oxide particles and Cr speciation was determined by performing micro X-ray fluorescence (μ-XRF) imaging analysis at Stanford Synchrotron Radiation Lightsource beamline 2-3 on pyrolusite and birnessite particles that were collected at the end of the experiments. The chromium hotspots that were identified via μ-XRF imaging were then analyzed using μ-XANES analysis to determine the Cr oxidation state.

To prepare samples for μ-XRF analysis, anoxically dried solid samples from the Mn oxide-containing chamber were embedded in the adhesive Loctite 404 in a 1.5 mL centrifuge tube under anoxic conditions (O_2 < 1 ppmv (ppm by volume), H_2 ~ 3.5%) and allowed to cure for >24 h. Loctite is relatively free of impurities, and μ-XRF analysis of the Loctite matrix revealed no noticeable background for Cr, Mn, or Fe. The bottom of the centrifuge tubes and samples were cut and glued to a 2 in. × 2 in. × 1 mm thick quartz slide (Ted Pella part no. 26012). The sample was then cut to a thickness of ~1 mm and polished to 100−200 μm, depending on the contact with the slide.

μ-XRF analysis was carried out at 6010 eV for total Cr, 7500 or 7150 eV for total Fe, and 7500 or 7150 eV for total Mn. The beam was calibrated to the pre-edge peak of Na_2CrO_4 at 5993 eV for Cr mapping. Multi-energy maps were collected on birnessite samples for Cr speciation (total Cr at 6010 eV and Cr(VI) at 5993 eV), Fe speciation (7122 eV intensity subtracted from intensity at 7130 eV representing Fe(III)) and Mn speciation (6559 eV subtracted from 6553 eV representing Mn(III) and 6562 eV subtracted from 6559 eV representing Mn(IV)) and processed using map math in the SMAK software.[43] Chromium μ-XANES spectral points were chosen based on the high Cr intensities detected in the total Cr μ-XRF maps. The μ-XANES spectra were then processed and analyzed using the same methods outlined for the bulk XANES analysis. Total Mn, Fe, and Cr maps were generated using the SMAK software.[43]

2.7. X-ray Photoelectron Spectroscopy Oxidation States. X-ray photoelectron spectroscopy (XPS) data were collected with a Kratos Axis Ultra DLD XPS instrument with an Al Kα monochromated X-ray source and a 165 mm electron energy hemispherical analyzer. All data were collected under a vacuum pressure below 3×10^{-9} Torr. The spectra were calibrated using the C 1s peak at 284.8 eV, and oxidation states were determined by comparing the observed peaks with peaks at known energies.

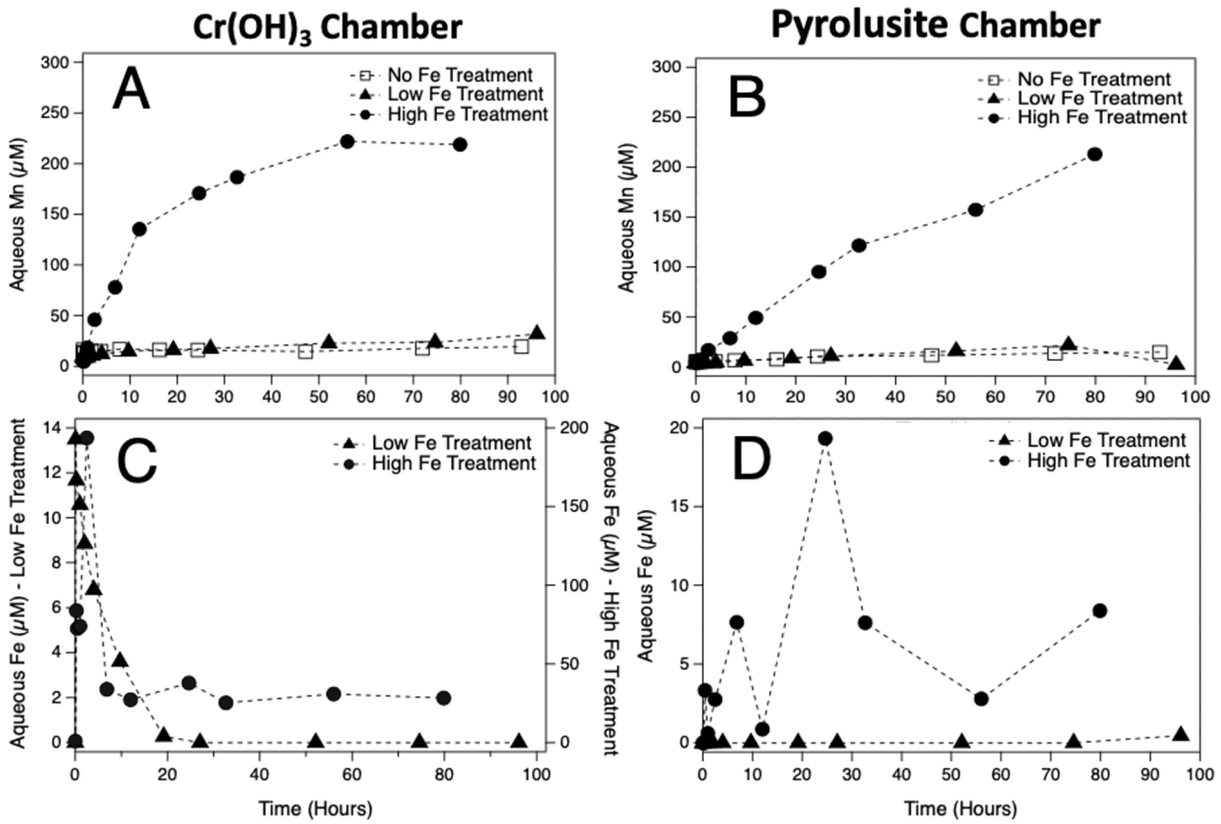

Figure 1. Concentration of dissolved (A, B) Mn and (C, D) Fe in the (A, C) $Cr(OH)_3$ and (B, D) pyrolusite reactor chambers. Fe(II) was added to the $Cr(OH)_3$ chamber to initiate the reaction. White squares, black triangles, and black circles represent no Fe(II) addition, low Fe(II) addition (14 μM), and high Fe(II) addition (100 μM), respectively. Note that the *y*-axis range for the aqueous Fe concentrations in (C) differs for the high (right axis) and low (left axis) treatments.

2.8. Diffusion Modeling. The Thiele modulus (ϕ)[29,31,44] was used to determine if reactions were diffusion-limited or reaction-limited (i.e., chemical kinetics) within the multichamber experiments. To estimate systems with first-order reaction rates and constant diffusivities, the following equation was used:

$$\phi = R\sqrt{k/D_e}$$

where R is the radius of the aggregate (mm), k is the first-order rate constant (s^{-1}), and D_e is the effective diffusivity of the of the aggregate ($mm^2\ s^{-1}$). If $\phi < 0.3$, the reaction is assumed to be kinetically limited, and if $\phi > 3$, the reaction is diffusion-limited. The half-length of the reactor used in these experiments was 70 mm.

To determine the rate of $Cr(OH)_3$ dissolution and subsequent diffusion of Cr(III) across the membrane, 2 g of $Cr(OH)_3$ was added to 750 mL of the background solution in one reactor chamber and allowed to equilibrate between the two chambers in the absence of Mn oxides and Fe(II). Aqueous samples from the adjacent chamber were collected over time and the total Cr was quantified using ICP-OES. Additional controls were conducted to determine the diffusion rate of Fe(II) at both high and low concentrations across the membrane without Mn oxides or Cr. The control experiments showed that the diffusion of Cr, Mn(II), and Fe(II) were very similar (Figures S3–S5). By applying the effective diffusivity that was calculated using the data acquired in the diffusion control experiments to calculate the Thiele modulus, we determined that all of the experiments conducted within the multichamber reactor were diffusion-limited rather than kinetically limited (Table S2).

3. RESULTS

3.1. Aqueous Fe and Mn Dynamics. We examined the chemical processes controlling the mobility of Cr and Mn at a diffusion-controlled redox interface by simulating the transport of reduced species from the interior of soil aggregates to the oxidizing exterior. Specifically, we examined the reaction products after the diffusion of added Fe(II) and Cr(III) solubilized from $Cr(OH)_3$ into a chamber containing Mn oxides (crystalline pyrolusite or poorly crystalline birnessite) using a multichamber reactor (Figure S1).

Relatively low (14 μM) or high (100 μM) concentrations of Fe(II) were added into the $Cr(OH)_3$ chamber to simulate the concentrations of Fe(II), a prevalent abiotic reductant, found in reducing zones of soil aggregates.[28,45] These concentrations were chosen because past studies have reported Fe(II) concentrations in aggregates ranging from 0 to 50 μM Fe(II) in the first 2 mm, 100–200 μM Fe(II) at 4 mm from the surface, and up to 250 μM in the center of the constructed aggregate.[45] In our reactors, the concentration of Fe decreased over the first 20 h of the reaction in the presence of low Fe(II) and remained below detection in both chambers for the remainder of the experiment (Figure 1C,D). In the high Fe(II) treatment, a steady state was reached after ~9 h with 30 ± 7 μM dissolved Fe remaining in both chambers for the remainder of the experiment (Figure 1C,D).

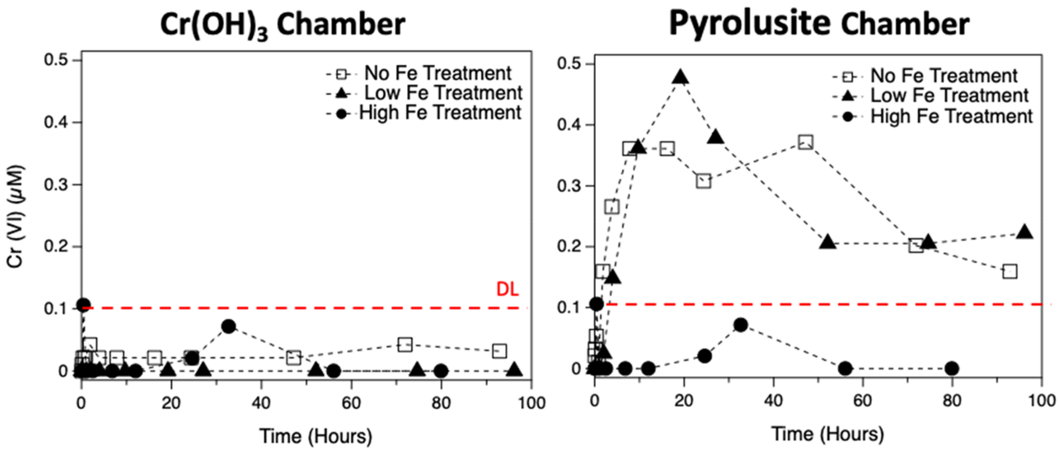

Figure 2. The aqueous concentration of Cr(VI) was determined by using a *s*-diphenyl carbazide (DPC) colorimetric assay in the chromium hydroxide and Fe(II) injection chamber (right panel) and the pyrolusite chamber (left panel) after the addition of no Fe(II) (white squares), low-concentration Fe(II) (14 μM, black triangles), and high-concentration Fe(II) (100 μM, black circles). The red dashed line represents the detection limit of the DPC colorimetric assay (0.1 μM).

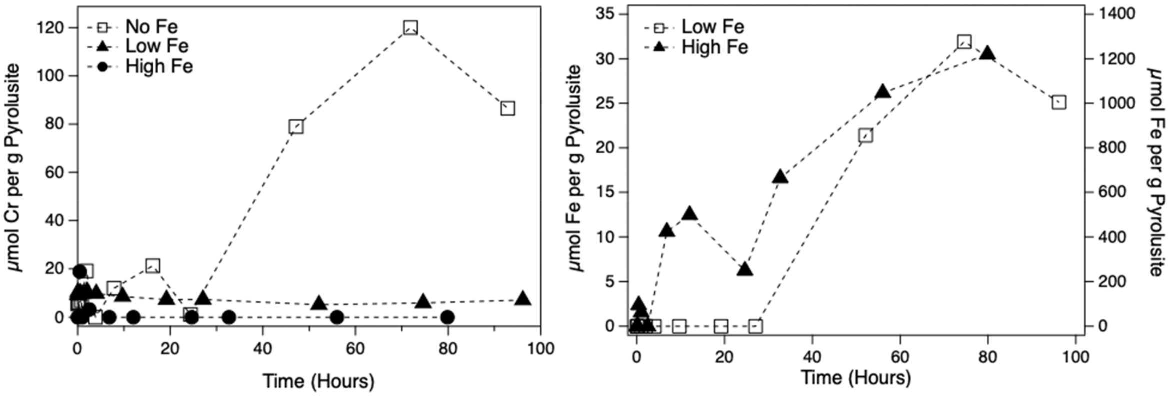

Figure 3. Solid concentration of chromium (right) and iron (left) per gram of pyrolusite after the addition of no Fe(II) (white squares), low-concentration Fe(II) (14 μM, black triangles), and high-concentration Fe(II) (100 μM, black circles), determined using acid digestion. The red dashed line represents the detection limit of the DPC colorimetric assay (0.1 μM).

The concentration of dissolved Mn (Mn_{aq}) in the pyrolusite chamber increased over the duration of the experiment under low and no Fe(II) treatments (Figure 1B). Mn_{aq} in the $Cr(OH)_3$ chamber at the end of the experiment was 47% higher with the addition of low-concentration Fe(II) (21.9 μM Mn_{aq}) than without the addition of Fe(II) (14.9 μM Mn_{aq}) (Figure 1A). The concentration of Mn_{aq} increased more rapidly in the presence of high-concentration Fe(II), being ~10 times higher (213 μM) than in the presence of low-concentration Fe(II) at 100 h (Figure 1A,B). The final concentration of Mn_{aq} between the chambers containing $Cr(OH)_3$ and pyrolusite was similar for all Fe treatments, demonstrating that the reaction proceeded until a steady state had been reached (Figure 1A,B).

3.2. Aqueous Cr Dynamics. Aqueous Cr(VI) generation was monitored in both chambers following the addition of Fe(II) to the $Cr(OH)_3$-containing chamber (Figure 2). The Cr(VI) dynamics with the no Fe(II) and low Fe(II) treatments were similar in the pyrolusite chamber. During the first 20 h of the experiment, the concentration of Cr(VI) with the addition of no Fe(II) and low-concentration Fe(II) increased from below detection (0.1 μM) to 0.36 and 0.47 μM Cr(VI), respectively; it then decreased to ~0.2 μM Cr(VI) between 60 and 100 h. In contrast, the concentration of Cr(VI) remained below the detection limit in the presence of high-concentration Fe(II) in the pyrolusite chamber. Cr(VI) was below the detection limit in the $Cr(OH)_3$ chamber for all experiments.

3.3. Chromium and Fe Sorption onto Mn Oxides. Pyrolusite solids were collected throughout the experiment and analyzed for solids associated with Fe and Cr (Figure 3). In the absence of Fe(II), 78−120 μmol of Cr g^{-1} of pyrolusite was detected on the pyrolusite solids after 60 h. In the low Fe(II) treatment, the amount of pyrolusite-associated Cr (~7 μmol of Cr g^{-1} of pyrolusite) was less than in the treatment without Fe(II), and it remained around the same level throughout the duration of the experiment. Pyrolusite-associated Cr was not detected in the high Fe(II) treatment experiment. The total amount of Fe was also measured on the solids in the pyrolusite chamber in both the high and low Fe(II) treatments. In the low Fe(II) treatment, Fe was not detected on the pyrolusite solids until 24 h, when it increased to ~21−31 μmol of Fe g^{-1} of pyrolusite. In the high Fe(II) treatment, Fe was detected less than an hour after its addition and increased to over 50 times (1220 μmol Fe g^{-1} pyrolusite) the amount of solids associated with Fe in the low Fe(II) treatment despite there being only a 7-fold difference in the initial Fe(II) concentration.

Next, XPS analysis was used to determine the Fe, Mn, and Cr speciation at the pyrolusite surfaces, and XAS was used to determine the bulk solid-phase speciation (Figures S8−S10). For both the low and high Fe(II) treatments, Fe $2p_{3/2}$ peaks were observed at around 710.9 eV, indicating the existence of Fe(III). Mn $2p_{3/2}$ peaks were observed at around 642 eV, which suggest the existence of Mn(IV) of MnO_2 in pyrolusite. The sole Cr $2p_{3/2}$ peak at 576.5 eV is assigned to Cr(III) rather than Cr(VI), which peaks at ∼580 eV. The XPS results indicate that surface-associated iron was oxidized to Fe(III) and surface-associated chromium was reduced to Cr(III); there was no indication of Cr(VI) in the XPS data. The relative atomic composition of the pyrolusite solids at the termination of the experiment in the low Fe(II) treatment was 3% Fe(III) and 3% Cr(III). In comparison, the pyrolusite solids that received high Fe(II) injection, the percent of Fe increased to 5% and Mn by 1% in relation to the total atomic composition on the pyrolusite surface.

At the termination of the experiment, X-ray absorption spectroscopy (XAS) analysis was completed on the pyrolusite solids to identify the types of Fe(III) (oxyhydr)oxides that were present in the pyrolusite solids. In the low Fe(II) treatment, the iron solids were mostly goethite (75%) with a smaller portion identified as hematite (22%). The high Fe(II) treatment had less goethite (52%) as well as ferrihydrite (43%) (Table S1 and Figure S7). No solids associated with Fe(II) were detected in the XAS measurements, which is consistent with the XPS data, thus indicating that the Fe on the solid surface was present only as oxidized Fe(III) solids (within the detection limit of these X-ray tools; see Figures S7 and S9). Mn K-edge XANES spectra revealed no average oxidation state (AOS) or structural changes in the pyrolusite in the absence of Fe(II) and in the low Fe(II) reactors (AOS ∼ 3.9, see Table 1). However, the AOS of pyrolusite decreased from 3.9 to 3.71 in the presence of high Fe(II) (Table 1).

Table 1. Average Oxidation State (AOS) of Pyrolusite prior to Initiation and at Termination[a]

	AOS at initiation	AOS at termination	decrease in AOS
no Fe	3.92	3.92	0
low Fe	3.99	3.96	0.03
high Fe	3.93	3.71	0.22

[a] Standards and fitting method from Manceau et al.[42]

To assess the spatial distribution and associations between Fe and Cr on Mn oxides, solids from the reactors were analyzed using synchrotron μ-XRF mapping and Cr K-edge μ-XANES at SSRL beamline 2-3 (Figure S11). Fe and Mn were spatially correlated in each treatment, providing evidence of near-complete Fe surface coverage of Mn oxide, which was similar to previous observations[18,21] (Figure S11). Chromium had a lower abundance and was more diffused than Fe and Mn. However, Cr in the high Fe treatment appeared to be more localized than in the low Fe treatment for both birnessite and pyrolusite (Figure 4). The XANES spectra of the sample areas containing the highest concentrations of Cr indicated that only Cr(III) was associated with solids based on the absence of a pre-edge feature diagnostic of Cr(VI) (Figure 4).

3.4. Effect of Mn Oxide Crystallinity on Cr and Fe Dynamics.

The effect of Mn oxide crystallinity on the oxidation of Cr and Fe in a diffusion-controlled environment was also observed (Figures 5 and 6). We replaced pyrolusite in the reactors with birnessite, a poorly crystalline Mn oxide that is more representative of the biogenic Mn oxides found in soils and aquifer materials.[20] In the absence of Fe(II), the concentration of Cr(VI) peaked at ∼20 h at approximately 3.2 μM and decreased to 1.7 μM after 60 h (Figure 6). The measured concentration of Cr(VI) after 20 h was 10 times higher than that measured in the pyrolusite reactors in the absence of Fe(II). The initial rate of Cr(III) oxidation differed in the presence of the two minerals. In the absence of Fe(II), the oxidation of Cr(III) by birnessite had an initial rate of 0.4 μM h^{-1}, which was ∼10 times higher than the initial rate of the oxidation of Cr(III) by pyrolusite (Figure 6 and Table S3).

When low concentrations of Fe(II) were injected into the reactor, the aqueous Cr(VI) dynamics within the birnessite chamber were different than in the presence of pyrolusite. The concentration of aqueous Cr(VI) peaked quickly at ∼20 min (1.4 μM) and then decreased until ∼20 h before plateauing at ∼0.25 μM Cr(VI), a concentration that was similar to the amount measured in the pyrolusite chamber with the low-concentration Fe(II) treatment (Figure 6). No Cr(VI) was detected in the $Cr(OH)_3$ chamber with either low or high Fe(II) treatments in the presence of either birnessite or pyrolusite. The aqueous Fe(II) dynamics were similar in the presence of both Mn oxides over the duration of the low Fe(II) experiment (Figure 5C,D). The Fe(II) concentration in the $Cr(OH)_3$ chamber peaked just after the addition of Fe(II); it then began to decrease until it was no longer detected after 20 h (Figure 5C). In the low Fe(II) treatment, aqueous Fe was not detected in the Mn oxide chamber for the duration of the experiment for both Mn oxide types (Figures 1D and 5D).

In the high Fe(II) and birnessite treatments, no Cr(VI) was detected in the birnessite chamber for the duration of the experiment (Figure 6). This result is similar to the Cr(VI) dynamics that were observed in the pyrolusite and high Fe(II) treatments. After the addition of high-concentration Fe(II), the aqueous Fe concentration peaked in both chambers immediately after the Fe addition and remained in solution for the duration of the experiment (Figure 5C,D). Aqueous iron was observed in the presence of both Mn oxide minerals when treated with high Fe(II) (Figures 1D and 5D). The concentration of aqueous Mn was highly variable in the birnessite chamber (Figure 5B). However, the aqueous Mn concentration in the $Cr(OH)_3$ chamber peaked at ∼10 h before decreasing for the remainder of the experiment (Figure 5A). Compared to the pyrolusite experiments, the concentration of Mn was ∼10 times less in the birnessite experiments (Figures 1B and 5B).

4. DISCUSSION

4.1. Competing Redox Processes that Limit Cr(VI) Production.

Our results indicate that Cr(III) oxidation by Mn(III/IV) oxides occurs in a diffusion-controlled system with inhibited physical interactions between the solid minerals. They also indicate that Cr(VI) generation is suppressed in the presence of high Fe(II), even in the presence of Mn oxides. The reaction sequence begins with the dissolution of $Cr(OH)_3$ and the diffusion of aqueous Cr(III) across the semipermeable membrane, where Cr(III) is oxidized by Mn oxides (pyrolusite or birnessite) to Cr(VI). These observations are consistent with the findings by Pan et al.,[10] where the birnessite-mediated oxidation of Cr(III) dissolved from $Cr(OH)_3$ occurred in a physically separated, diffusion-limited environment. Their study demonstrated that Mn oxide-driven Cr(III) oxidation was inhibited due to either the precipitation of $Cr(OH)_3$ on the Mn oxide surface or the precipitation of highly reactive Mn

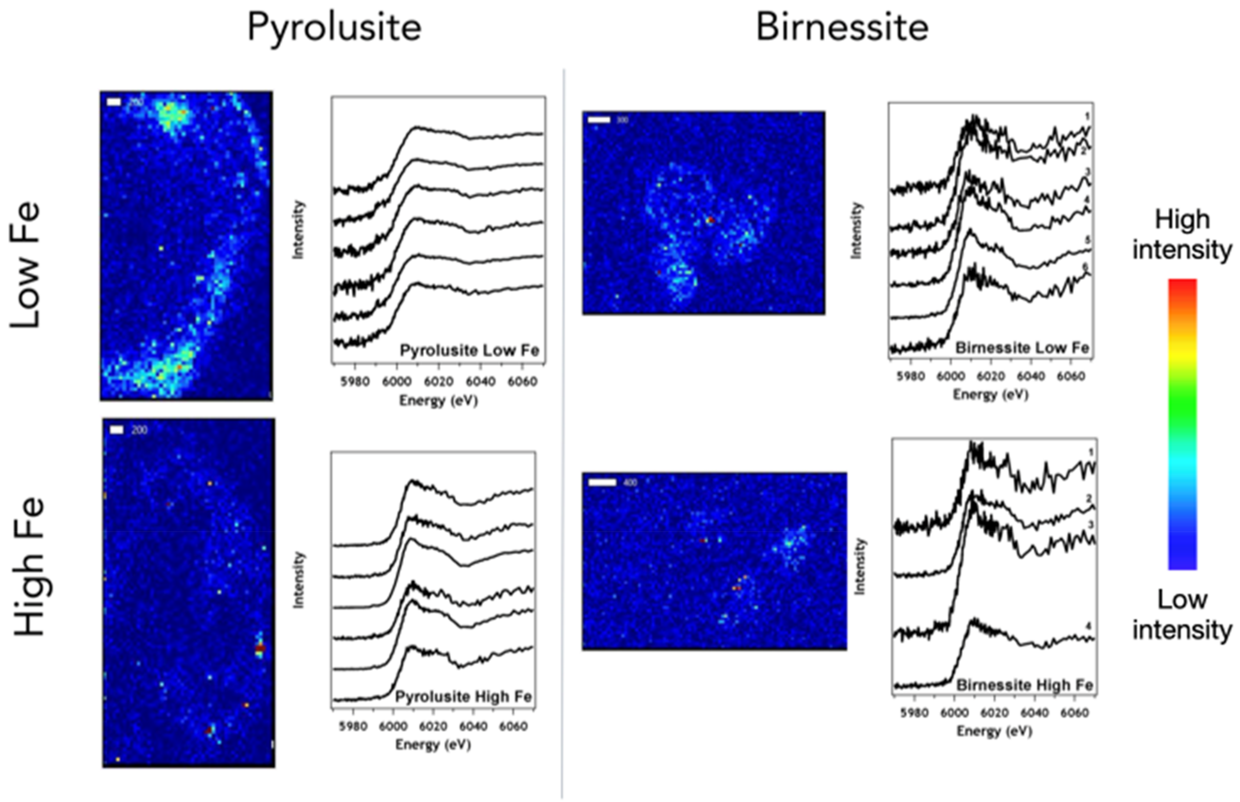

Figure 4. Cr μ-XRF maps and Cr K-edge μ-XANES spectra of pyrolusite and birnessite particles collected from the low Fe (top panels) and high Fe (bottom panels) treatment experiments. The colors on the μ-XRF maps represent the intensity of the Cr fluorescence signal in the sample sections, where blue represents relatively low Cr concentrations and red represents relatively high Cr concentrations (shown by the color gradient bar on the right). The Cr K-edge XANES spectra show that Cr(VI) was not detected on the surface of birnessite particles at multiple locations surveyed.

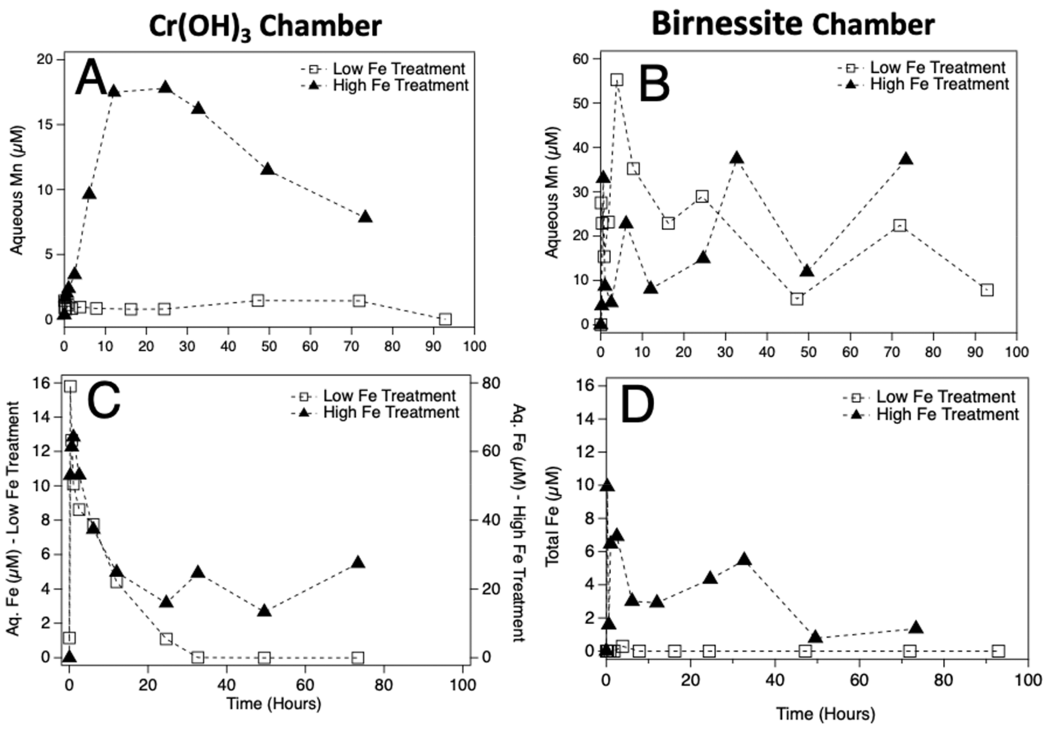

Figure 5. Concentration of dissolved (A, B) Mn and (C, D) Fe in the (A, C) $Cr(OH)_3$ and (B, D) birnessite reactor chambers. Fe(II) was added to the $Cr(OH)_3$ chamber to initiate the reaction. White squares, black triangles, and black circles represent no Fe(II) addition, low Fe(II) addition (14 μM), and high Fe(II) addition (100 μM), respectively. Note that the y-axis range for the concentration of aqueous Fe in (C) differs for the high (right axis) and low (left axis) treatments.

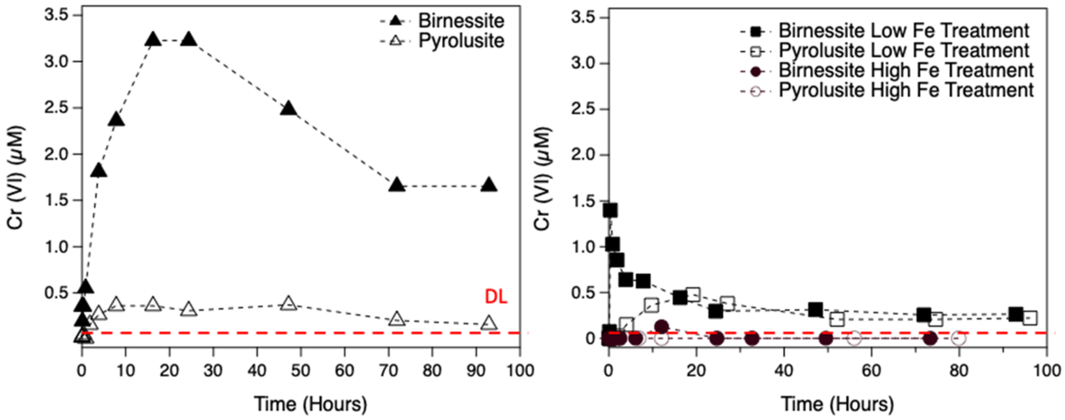

Figure 6. Aqueous concentration of Cr(VI) measured by DPC assay in the Mn oxide chamber when using highly crystalline pyrolusite (white symbols) and poorly crystalline birnessite (black symbols) after the addition of no Fe(II) (left) and low-concentration Fe(II) (14 μM; right). The red dashed line represents the detection limit of the DPC colorimetric assay (0.1 μM).

oxides in ambient oxygen conditions. Furthermore, Pan et al. found no adsorbed Cr(VI) on Mn oxides; however, adsorbed Cr(VI) was found on $Cr_xFe_{1-x}(OH)_3$ minerals at lower pH.

Because Cr(VI) generation can also occur under reducing conditions,[46−48] we also investigated the fate of Cr in the presence of both an oxidant (Mn oxide) and a reductant (Fe(II)). Aqueous Fe(II) was added to the Cr chamber and diffused into the Mn chamber. In the diffusion-controlled reactors, the oxidation of Cr(III) in the presence of 14 μM Fe(II) was similar to the control with no Fe. However, the oxidation of Cr(III) to Cr(VI) was not observed in the presence of 100 μM Fe(II). Within our systems, Fe(II) remained aqueous but was also likely adsorbed to $CrOH_3$, the Mn oxides, or newly formed Fe oxides, all of which could have contributed to Cr(VI) reduction pathways. Therefore, a combination of three possible mechanisms may explain the decrease of Cr(VI): (i) the passivation of the Mn oxide surfaces by the oxidation of Fe(II) and the precipitation of Fe(III) minerals;[21] (ii) the adsorption of aqueous species onto the Mn oxides, which blocks adsorption sites; or (iii) the direct reduction of Cr(VI) by aqueous or adsorbed Fe(II).[39,49,50]

Solid-phase analysis at the termination of the reactors indicated the likely formation of Fe(III) oxyhydroxides on the Mn oxide surfaces and that more Fe(III) was associated with the high Fe(II) treatment. In previous studies, it has been determined that Mn oxide mineralogy likely changes in the presence of Fe(II). When observing As(III) oxidation by birnessite, the oxidation capacity of the mineral was found to diminish at higher As concentrations, likely due to the barrier formed by As(V) that prevents further oxidation by interior Mn(IV).[36,51,52] Within our systems, Fe(II) is likely forming a barrier and slowing or preventing further Cr(III) oxidation. This behavior is similar to that found by Mock et al.,[21] who determined that Fe(II) oxidation by Mn oxides and the subsequent formation of Fe(III) oxyhydroxides on Mn oxide surfaces suppresses the oxidative capacity of Mn oxides toward reduced species, such as arsenic.

The Fe(III) oxyhydroxides that formed on the surface of pyrolusite were primarily goethite (Table S1). This may be due to the lower surface area of pyrolusite, as having a more complete coverage of the available surface area leads to a Fe(II)-driven transformation of the initially precipitated, more poorly crystalline Fe(III) hydroxides. In previous works, the further reaction of Fe(III) oxyhydroxides with any remaining Fe(II) resulted in the formation of the more crystalline Fe(III) oxyhydroxide goethite.[53,54] Schaefer et al.[18] demonstrated that Fe oxide coatings formed through the abiotic reaction of Fe(II) with pyrolusite resulted initially in lepidocrocite, but the continued reaction with Fe(II) resulted in the partial reduction of lepidocrocite to magnetite and a release of additional aqueous Mn. Surface passivation by Fe(III) mineral precipitation likely contributed to the suppression of Cr(III) oxidation by blocking reactive sites on the Mn oxide surface.

In the high Fe(II) treatments, high concentrations of aqueous Mn(II) were detected due to the reductive dissolution of the Mn oxide solids (Figures 1 and 5). Elzinga[55] determined that aqueous Mn(II) sorption and comproportionation with structural Mn(IV) forms Mn(III) within a Mn oxide sheet. Such changes in the crystalline structure of Mn oxides can decrease their sorption and redox activity. While there was a slight decrease in the AOS in the birnessite reactors, the AOS of the pyrolusite solids at the termination of the high Fe(II) treatment was lower due to the higher concentration of aqueous Mn(II) that was detected in the rectors and the occurance of Mn(II) sorption onto the mineral. Because AOS is a bulk measurement of Mn speciation, the decrease in the average oxidation state may be due to either dissolved Mn(II) reacting back with the Mn oxide surface or the reduction of Mn(IV) without dissolution.[56,57]

Aside from Mn reduction, $Fe(II)_{aq}$ can directly reduce $Cr(VI)_{aq}$ through a homogeneous reaction.[39,49,50,58] In the low $Fe(II)_{aq}$ treatments, Fe_{aq} was below the detection limit in both chambers after 20 h because the added Fe(II) was precipitated as Fe(III) oxides. However, in the high Fe treatments, $Fe(II)_{aq}$ remained in solution for the duration of the experiment (Figures 1 and 5). Previous studies have shown that relatively low concentrations of $Fe(II)_{aq}$ (e.g., 10 μM) can reduce $Cr(VI)_{aq}$ under environmental conditions,[49] which would inhibit the accumulation of Cr(VI) in high Fe treatments. The fact that the concentration of $Fe(II)_{aq}$ was sustained also indicated that Fe(II) had equilibrated with the initial Mn oxide solids. However, in our system, Fe(II) was also likely adsorbed to $CrOH_3$, the Mn oxides, or newly formed Fe oxides.

The amount of $Cr(VI)_{aq}$ that was generated in the multiple experimental iterations was greater than the public health goal (PHG) of 0.05 $\mu g\ L^{-1}$ for Cr(VI) set by the California Office of Environmental Health Hazard Assessment.[59] The amount of Cr(VI) that was detected in the pyrolusite and birnessite reactors without Fe(II) was ~900 and ~8000 times higher than the public health goal, respectively. Currently, an enforceable maximum contaminant level (MCL) only exists for total chromium. The World Health Organization (WHO)[60] sets its recommended guideline value for total chromium at 50 μg $L^{-1,}$ and the MCL set by the U.S. Environmental Protection Agency[61] is 100 μg L^{-1}.

No primary or enforceable MCL exists for Mn despite increasing evidence of its toxicity at high concentrations, although the World Health Organization has a provisional health-based guideline of 80 μg L^{-1}.[62,63] All pyrolusite treatments exceeded the exposure threshold that links Mn(II) exposure in drinking water to neurotoxic effects in children[64−66] (120 μg L^{-1}). The highest amount of $Mn(II)_{aq}$, which was ~130 times higher than the WHO provisional guideline, was detected in the high Fe pyrolusite treatment and was .

4.2. Impact of Mn Oxide Crystallinity. To evaluate the effect of Mn oxide crystallinity on the Fe(II) and Cr(III) oxidation reactions, we compared crystalline, low specific surface area (SSA) pyrolusite (6.23 m^2/g) to poorly crystalline, high SSA birnessite (37.8 m^2/g). Both surface area and crystallinity influence the reactivity and oxidative capacity of Mn oxide.[67] Pyrolusite is the most thermodynamically stable Mn oxide and represents an end-member case for Mn(IV) reduction by $Fe(II)_{aq}$. If Cr(III) oxidation occurs with pyrolusite, it is likely to occur with other Mn oxides as well. However, birnessite was included as a comparison, as it more closely resembles the biogenic Mn oxides that are abundant in soils and aquifers.[9,47,68] It should also be noted that PIPES buffer, which was used in these systems, has been identified as a potential modifier of the Mn(III) content of Mn oxide minerals and, therefore, their reactivity.[69] Therefore, the reactions that were observed reflect the cumulative effects of all reactants in the reaction system, including the PIPES buffer.

As expected from prior studies, the Cr(III) reaction with birnessite generated higher concentrations of Cr(VI) than that with pyrolusite when under similar initial conditions due to the higher surface area of birnessite.[70] Both pyrolusite and birnessite oxidized aqueous Fe(II), resulting in Fe(III) (oxyhydr)oxide surface precipitation; however, the larger surface area of birnessite resulted in incomplete surface coverage. Similar results have been observed for complete surface coverage for pyrolusite at higher Fe(II) concentrations[18] and incomplete surface coverage for birnessite.[21] In the low Fe(II) birnessite treatment, the cumulative generation of Cr(VI) was ~3 times higher than in the pyrolusite treatment, which may be attributed to the faster initial rate of Cr(III) oxidation in the first ~20 h before more of the surface (but not the entire surface) was covered by Fe(III) oxyhydroxides on the birnessite surface.

The solubility of the Cr-bearing mineral also plays an essential role in the production of Cr(VI) in diffusion-limited environments. In the environment, Fe(II)-mediated Cr(VI) reduction results in the formation of the Cr(III)−Fe(III) co-precipitate $Cr_xFe_{1-x}(OH)_3$, which is less soluble than pure $Cr(OH)_3$.[24,71,72] In previous studies that investigated the impact of lower-solubility Cr-bearing minerals, Cr(VI) generation was proportional to the mineral solubility.[9−11,47,73] Although Fe-substituted Cr minerals were not investigated in this study, the dissolution of $Cr(OH)_3$ and the migration of $Cr(III)_{aq}$ to the Mn oxide surface were the initial rate-limiting step in the production of Cr(VI) within this system (Table S3). Mineral substitution of Fe that results in decreased Cr(III) mineral solubility would only further limit the diffusive flux to the Mn oxides and decrease the production rate of Cr(VI).

4.3. Diffusion Controls on Redox Reactions. In the environment, reducing conditions may occur in the interior of soil aggregates where the oxygen demand exceeds the oxygen supplied via diffusion from the surface of the aggregates.[28,29,38] Reduced Fe(II) from the anoxic, biotic reduction of Fe oxides in the aggregate interiors then diffuses toward zones of Cr(VI) generation (aggregate exterior), all while maintaining physical separation between the mineral solids.[31] Similarly, Cr(III) solids and Mn oxides may be physically separated in the environment, so the reaction is also dependent on the rate of Cr(III) dissolution from the solid mineral and diffusion to the site of oxidation.[6] All experiments presented herein were diffusion-controlled based on Thiele modulus calculations (Table S2). We were then able to observe the impacts of Fe(II) diffusion to zones of Cr(VI) generation while maintaining the physical separation of $Cr(OH)_3$ and Mn oxides, similar to the physical limitations observed in soil aggregates. Prior studies have shown that the solubility of the Cr(III)-bearing minerals combined with the distance that the dissolved Cr(III) must travel to reach the Mn oxides determines the production rate of Cr(VI).[9−11]

Physical separation, yet proximity, of secondary Cr(III) minerals to Mn oxides has been observed in serpentine soils.[68,74] Within these environments, the dissolution of Cr(III) from Cr-bearing minerals and the diffusion of Cr(III) to oxidative minerals like Mn oxides play an essential role in the net production and transport of Cr(VI) into groundwater. However, the Cr(VI) that has been measured in infiltrating water was attenuated while flowing to surface water sources due to dilution by infiltration water or reduction via microbial activity or Fe(II).[68,74] Our study demonstrates that the presence of Fe(II) may inhibit Cr(VI) transport through both the oxidative precipitation of Cr(VI) itself and the reduction of Mn oxides, which are responsible for much of the Cr(III) oxidation seen in aquifer systems.

5. CONCLUSIONS

The processes controlling Cr cycling in soil environments are complex and site-specific. Mn and Fe oxides commonly exist in many soil environments and, due to their redox activity, it is important to understand how both play a role in the oxidative release of toxic groundwater contaminants such as Cr(VI). This work demonstrated that despite diffusion limitations, the physical separation of solid minerals and the introduction of competing reactants in environmentally relevant concentrations, Cr(VI) and Mn(II) can be generated at concentrations exceeding regulatory levels in model systems. The release and outward diffusion of Fe(II) from the anaerobic centers of soil aggregates represent a pathway for the release of a competing reactant in well-aerated soil environments that may fully disrupt the oxidation of Cr(III). However, the extent of Cr(III) oxidation by Mn oxides was observed to be dependent on the Fe(II) concentration and Mn oxide mineralogy.

Despite evidence of less Cr(III) oxidation occurring in the presence of co-occurring reactants, such as Fe(II), there is still evidence of large-scale Cr(VI) transport into groundwater.[68,75] Therefore, it is essential to note that the transport of Cr(VI) into advecting water is highly scale-dependent. The specific biogeochemical characteristics of local environments such as anoxic zones, microbial activity, and mineral solubilities must be considered when investigating the potential for geogenic metal release into groundwater in specific environments.

ASSOCIATED CONTENT

Supporting Information

The Supporting Information is available free of charge at https://pubs.acs.org/doi/10.1021/acsearthspacechem.3c00141.

> XRD data for birnessite and pyrolusite; reactor schematic; control reactors experiments; solid-phase experiments; X-ray absorption spectra for iron; XPS spectra for Cr, Mn, and Fe; μ-XRF mapping of Mn and Fe; diffusion coefficient calculations; Thiele modulus calculations; and reaction rates of Cr(III) oxidation and Mn(II) dissolution (PDF)

AUTHOR INFORMATION

Corresponding Author

Samantha C. Ying − *School of Earth and Environmental Sciences, Schmid College of Science and Technology, Chapman University, Orange, California 92866, United States; Department of Environmental Sciences, University of California, Riverside, Riverside, California 92521, United States*; orcid.org/0000-0002-1247-2529; Email: samying@ucr.edu

Authors

Miranda L. Aiken − *School of Earth and Environmental Sciences, Schmid College of Science and Technology, Chapman University, Orange, California 92866, United States*; orcid.org/0000-0002-1692-2056

Macon J. Abernathy − *SLAC National Accelerator Laboratory, Menlo Park, California 94025, United States*; orcid.org/0000-0002-0455-2086

Michael V. Schaefer − *Department of Earth and Environmental Science, New Mexico Tech, Socorro, New Mexico 87801, United States*; orcid.org/0000-0001-6255-3362

Ilkeun Lee − *Department of Chemistry, University of California, Riverside, Riverside, California 92521, United States*; orcid.org/0000-0001-5718-7898

Complete contact information is available at: https://pubs.acs.org/10.1021/acsearthspacechem.3c00141

Notes

The authors declare no competing financial interest.

ACKNOWLEDGMENTS

The authors express endless gratitude to those who made this work possible. This includes, but is not limited to, Sam Webb, Matthew Latimer, Erik Nelson, and Ryan Davis at Stanford Synchrotron Radiation Lightsource (SSRL) for assisting with setting up and troubleshooting the XAS data collection process, as well as David Lyons at UCR for his help with the aqueous ICP-OES analysis. Portions of this research were completed at Stanford Synchrotron Radiation Laboratory, a directorate of the SLAC National Accelerator Laboratory and an Office of Science User Facility operated for the U.S. Department of Energy Office of Science by Stanford University. Use of the Stanford Synchrotron Radiation Lightsource, SLAC National Accelerator Laboratory, is supported by the U.S. Department of Energy, Office of Science, Office of Basic Energy Sciences under Contract No. DE-AC02-76SF00515. The authors also thank the family, friends, and co-workers in the Dirty Lab.

REFERENCES

(1) Costa, M.; Klein, C. B. Toxicity and Carcinogenicity of Chromium Compounds in Humans. *Critical Reviews in Toxicology* **2006**, *36* (2), 155−163.

(2) Ball, J. W.; Nordstrom, D. K. Critical Evaluation and Selection of Standard State Thermodynamic Properties for Chromium Metal and Its Aqueous Ions, Hydrolysis Species, Oxides, and Hydroxides. *J. Chem. Eng. Data* **1998**, *43* (6), 895−918.

(3) Richard, F. C.; Bourg, A. C. M. Aqueous Geochemistry of Chromium: A Review. *Water Res.* **1991**, *25* (7), 807−816.

(4) Zhitkovich, A. Chromium in Drinking Water: Sources, Metabolism, and Cancer Risks. *Chem. Res. Toxicol.* **2011**, *24* (10), 1617−1629.

(5) Rai, D.; Sass, B.; Moore, D. Chromitim(III) Hydrolysis Constants and Solubility of Chromium(III) Hydroxide. *Inorg. Chem.* **1987**, *26* (3), 345−349.

(6) Oze, C.; Bird, D. K.; Fendorf, S. Genesis of Hexavalent Chromium from Natural Sources in Soil and Groundwater. *Proc. Natl. Acad. Sci. U.S.A.* **2007**, *104* (16), 6544−6549.

(7) Hausladen, D. M.; Alexander-Ozinskas, A.; McClain, C.; Fendorf, S. Hexavalent Chromium Sources and Distribution in California Groundwater. *Environ. Sci. Technol.* **2018**, *52*, 8242.

(8) Oze, C.; Fendorf, S.; Bird, D. K.; Coleman, R. G. Chromium Geochemistry of Serpentine Soils. *International Geology Review* **2004**, *46* (2), 97−126.

(9) Hausladen, D. M.; Fendorf, S. Hexavalent Chromium Generation within Naturally Structured Soils and Sediments. *Environ. Sci. Technol.* **2017**, *51* (4), 2058−2067.

(10) Pan, C.; Liu, H.; Catalano, J. G.; Wang, Z.; Qian, A.; Giammar, D. E. Understanding the Roles of Dissolution and Diffusion in Cr(OH)3 Oxidation by δ-MnO2. *ACS Earth Space Chem.* **2019**, *3* (3), 357−365.

(11) Pan, C.; Liu, H.; Catalano, J. G.; Qian, A.; Wang, Z.; Giammar, D. E. Rates of Cr(VI) Generation from CrxFe1-x(OH)3 Solids upon Reaction with Manganese Oxide. *Environ. Sci. Technol.* **2017**, *51* (21), 12416−12423.

(12) Murray, K. J.; Mozafarzadeh, M. L.; Tebo, B. M. Cr(III) Oxidation and Cr Toxicity in Cultures of the Manganese(II)-Oxidizing Pseudomonas Putida Strain GB-1. *Geomicrobiology Journal* **2005**, *22* (3−4), 151−159.

(13) Fendorf, S.; Zasoski, R. Chromium (III) Oxidation by. Delta.-Manganese Oxide (MnO2). 1. Characterization. *Environ. Sci. Technol.* **1992**, *26* (1), 79−85.

(14) Eary, L. E.; Rai, D. Chromate Reduction by Subsurface Soils under Acidic Conditions. *Soil Science Society of America Journal* **1991**, *55* (3), 676−683.

(15) Mc Kenzie, R. M. Manganese Oxides and Hydroxides. In *Minerals in Soil Environments*; John Wiley & Sons, Ltd., 1989; p 439−465. DOI: 10.2136/sssabookser1.2ed.c9.

(16) Post, J. E. Crystal Structures of Manganese Oxide Minerals. *Catena, Supplement* **1992**, *21*, 51−73.

(17) O'Reilly, S. E.; Hochella, M. F. Lead Sorption Efficiencies of Natural and Synthetic Mn and Fe-Oxides. *Geochim. Cosmochim. Acta* **2003**, *67* (23), 4471−4487.

(18) Schaefer, M. V.; Handler, R. M.; Scherer, M. M. Fe(II) Reduction of Pyrolusite (β-MnO2) and Secondary Mineral Evolution. *Geochemical Transactions* **2017**, *18* (1), 7.

(19) Weaver, R. M.; Hochella, M. F. Jr. The Reactivity of Seven Mn-Oxides with Cr3+aq: A Comparative Analysis of a Complex, Environmentally Important Redox Reaction. *Am. Mineral.* **2003**, *88* (11−12), 2016−2027.

(20) Tebo, B. M.; Bargar, J. R.; Clement, B. G.; Dick, G. J.; Murray, K. J.; Parker, D.; Verity, R.; Webb, S. M. Biogenic Manganese Oxides:

Properties and Mechanisms of Formation. *Annual Review of Earth and Planetary Sciences* **2004**, *32*, 287−328.

(21) Mock, R. P.; Schaefer, M. V.; Pacheco, J. L.; Lake, L.; Lee, I.; Ying, S. C. Influence of Fe(II) on Arsenic(III) Oxidation by Birnessite in Diffusion-Limited Systems. *ACS Earth Space Chemistry* **2019**, *3* (4), 550−561.

(22) Ying, S. C.; Kocar, B. D.; Griffis, S. D.; Fendorf, S. Competitive Microbially and Mn Oxide Mediated Redox Processes Controlling Arsenic Speciation and Partitioning. *Environ. Sci. Technol.* **2011**, *45* (13), 5572−5579.

(23) Wu, Y.; Li, W.; Sparks, D. L. The Effects of Iron(II) on the Kinetics of Arsenic Oxidation and Sorption on Manganese Oxides. *J. Colloid Interface Sci.* **2015**, *457*, 319−328.

(24) Sass, B.; Rai, D. Solubility of Amorphous Chromium(III)-Iron(III) Hydroxide Solid Solutions. *Inorg. Chem.* **1987**, *26* (14), 2228−2232.

(25) Gerke, H. H. Preferential Flow Descriptions for Structured Soils. *Journal of Plant Nutrition and Soil Science* **2006**, *169* (3), 382−400.

(26) Zausig, J.; Stepniewski, W.; Horn, R. Oxygen Concentration and Redox Potential Gradients in Unsaturated Model Soil Aggregates. *Soil Science Society of America Journal* **1993**, *57* (4), 908−916.

(27) Sexstone, A. J.; Revsbech, N. P.; Parkin, T. B.; Tiedje, J. M. Direct Measurement of Oxygen Profiles and Denitrification Rates in Soil Aggregates 1. *Soil Science Society of America Journal* **1985**, *49* (3), 645−651.

(28) Masue-Slowey, Y.; Ying, S. C.; Kocar, B. D.; Pallud, C. E.; Fendorf, S. Dependence of Arsenic Fate and Transport on Biogeochemical Heterogeneity Arising from the Physical Structure of Soils and Sediments. *Journal Environmental Quality* **2013**, *42* (4), 1119−1129.

(29) Ying, S. C.; Masue-Slowey, Y.; Kocar, B. D.; Griffis, S. D.; Webb, S.; Marcus, M. A.; Francis, C. A.; Fendorf, S. Distributed Microbially- and Chemically-Mediated Redox Processes Controlling Arsenic Dynamics within Mn-/Fe-Oxide Constructed Aggregates. *Geochim. Cosmochim. Acta* **2013**, *104*, 29−41.

(30) Tokunaga, T. K.; Wan, J.; Hazen, T. C.; Schwartz, E.; Firestone, M. K.; Sutton, S. R.; Newville, M.; Olson, K. R.; Lanzirotti, A.; Rao, W. Distribution of Chromium Contamination and Microbial Activity in Soil Aggregates. *Journal of Environmental Quality* **2003**, *32* (2), 541−549.

(31) Tokunaga, T. K.; Wan, J.; Firestone, M. K.; Hazen, T. C.; Schwartz, E.; Sutton, S. R.; Newville, M. Chromium Diffusion and Reduction in Soil Aggregates. *Environ. Sci. Technol.* **2001**, *35* (15), 3169−3174.

(32) Gonzalez, A. R.; Ndung'u, K.; Flegal, A. R. Natural Occurrence of Hexavalent Chromium in the Aromas Red Sands Aquifer, California. *Environ. Sci. Technol.* **2005**, *39* (15), 5505−5511.

(33) Ndung'u, K.; Friedrich, S.; Gonzalez, A. R.; Flegal, A. R. Chromium Oxidation by Manganese (Hydr)Oxides in a California Aquifer. *Appl. Geochem.* **2010**, *25* (3), 377−381.

(34) Hansel, C. M.; Wielinga, B. W.; Fendorf, S. Structural and Compositional Evolution of Cr/Fe Solids after Indirect Chromate Reduction by Dissimilatory Iron-Reducing Bacteria. *Geochim. Cosmochim. Acta* **2003**, *67* (3), 401−412.

(35) McKenzie, R. M. The Synthesis of Birnessite, Cryptomelane, and Some Other Oxides and Hydroxides of Manganese. *Mineralogical Magazine* **1971**, *38* (296), 493−502.

(36) Ying, S. C.; Kocar, B. D.; Fendorf, S. Oxidation and Competitive Retention of Arsenic between Iron- and Manganese Oxides. *Geochim. Cosmochim. Acta* **2012**, *96*, 294−303.

(37) Tufano, K. J.; Reyes, C.; Saltikov, C. W.; Fendorf, S. Reductive Processes Controlling Arsenic Retention: Revealing the Relative Importance of Iron and Arsenic Reduction. *Environ. Sci. Technol.* **2008**, *42* (22), 8283−8289.

(38) Pallud, C.; Kausch, M.; Fendorf, S.; Meile, C. Spatial Patterns and Modeling of Reductive Ferrihydrite Transformation Observed in Artificial Soil Aggregates. *Environ. Sci. Technol.* **2010**, *44* (1), 74−79.

(39) Buerge, I. J.; Hug, S. J. Kinetics and PH Dependence of Chromium(VI) Reduction by Iron(II). *Environ. Sci. Technol.* **1997**, *31* (5), 1426−1432.

(40) Bartlett, R.; James, B. Behavior of Chromium in Soils: III. Oxidation. *Journal of Environmental Quality* **1979**, *8* (1), 31−35.

(41) Ravel, B.; Newville, M. ATHENA, ARTEMIS, HEPHAESTUS: Data Analysis for X-Ray Absorption Spectroscopy Using IFEFFIT. *Journal Synchrotron Radiation* **2005**, *12* (4), 537−541.

(42) Manceau, A.; Marcus, M. A.; Grangeon, S. Determination of Mn Valence States in Mixed-Valent Manganates by XANES Spectroscopy. *Am. Mineral.* **2012**, *97* (5−6), 816−827.

(43) Webb, S. M. SIXpack: A Graphical User Interface for XAS Analysis Using IFEFFIT. *Phys. Scr.* **2005**, *2005* (T115), 1011.

(44) Thiele, E. W. Relation between Catalytic Activity and Size of Particle. *Ind. Eng. Chem. Res.* **1939**, *31* (7), 916−920.

(45) Masue-Slowey, Y.; Kocar, B. D.; Bea Jofré, S. A.; Mayer, K. U.; Fendorf, S. Transport Implications Resulting from Internal Redistribution of Arsenic and Iron within Constructed Soil Aggregates. *Environ. Sci. Technol.* **2011**, *45* (2), 582−588.

(46) Ao, M.; Sun, S.; Deng, T.; Zhang, F.; Liu, T.; Tang, Y.; Li, J.; Wang, S.; Qiu, R. Natural Source of Cr(VI) in Soil: The Anoxic Oxidation of Cr(III) by Mn Oxides. *Journal of Hazardous Materials* **2022**, *433*, 128805.

(47) Oze, C.; Sleep, N. H.; Coleman, R. G.; Fendorf, S. Anoxic Oxidation of Chromium. *Geology* **2016**, *44* (7), 543−546.

(48) Johnson, C. A.; Sigg, L.; Lindauer, U. The Chromium Cycle in a Seasonally Anoxic Lake. *Limnology and Oceanography* **1992**, *37* (2), 315−321.

(49) Fendorf, S.; Li, G. Kinetics of Chromate Reduction by Ferrous Iron. *Environ. Sci. Technol.* **1996**, *30* (5), 1614−1617.

(50) Buerge, I. J.; Hug, S. J. Influence of Mineral Surfaces on Chromium(VI) Reduction by Iron(II). *Environ. Sci. Technol.* **1999**, *33* (23), 4285−4291.

(51) Oscarson, D. W.; Huang, P. M.; Liaw, W. K. Role of Manganese in the Oxidation of Arsenite by Freshwater Lake Sediments. *Clays and Clay Minerals* **1981**, *29* (3), 219−225.

(52) Manning, B. A.; Fendorf, S. E.; Bostick, B.; Suarez, D. L. Arsenic(III) Oxidation and Arsenic(V) Adsorption Reactions on Synthetic Birnessite. *Environ. Sci. Technol.* **2002**, *36* (5), 976−981.

(53) Hansel, C. M.; Benner, S. G.; Neiss, J.; Dohnalkova, A.; Kukkadapu, R. K.; Fendorf, S. Secondary Mineralization Pathways Induced by Dissimilatory Iron Reduction of Ferrihydrite under Advective Flow. *Geochim. Cosmochim. Acta* **2003**, *67* (16), 2977−2992.

(54) Hansel, C. M.; Benner, S. G.; Fendorf, S. Competing Fe(II)-Induced Mineralization Pathways of Ferrihydrite. *Environ. Sci. Technol.* **2005**, *39* (18), 7147−7153.

(55) Elzinga, E. J. Reductive Transformation of Birnessite by Aqueous Mn(II). *Environ. Sci. Technol.* **2011**, *45* (15), 6366−6372.

(56) Elzinga, E. J. (54)Mn Radiotracers Demonstrate Continuous Dissolution and Reprecipitation of Vernadite (δ-MnO2) during Interaction with Aqueous Mn(II). *Environ. Sci. Technol.* **2016**, *50* (16), 8670−8677.

(57) Learman, D. R.; Voelker, B. M.; Vazquez-Rodriguez, A. I.; Hansel, C. M. Formation of Manganese Oxides by Bacterially Generated Superoxide. *Nature Geoscience* **2011**, *4* (2), 95−98.

(58) Ginder-Vogel, M.; Borch, T.; Mayes, M. A.; Jardine, P. M.; Fendorf, S. Chromate Reduction and Retention Processes within Arid Subsurface Environments. *Environ. Sci. Technol.* **2005**, *39* (20), 7833−7839.

(59) *Final Public Health Goal for Hexavalent Chromium*; Office of the Environmental Health Hazard Assessment, 2011.

(60) *Guidelines for Drinking-Water Quality* 3rd ed.; World Health Organization, 2008; Vol *1*. https://www.who.int/publications/i/item/9789241547611.

(61) Chromium in Drinking Water. United States Environmental Protection Agency. https://www.epa.gov/sdwa/chromium-drinking-water (accessed 2023-05-22).

(62) Coetzee, D. J.; McGovern, P. M.; Rao, R.; Harnack, L. J.; Georgieff, M. K.; Stepanov, I. Measuring the Impact of Manganese Exposure on Children's Neurodevelopment: Advances and Research Gaps in Biomarker-Based Approaches. *Environmental Health* **2016**, *15* (1), 91.

(63) *Guidelines for Drinking-Water Quality* 4th ed.; World Health Organization, 2022. https://www.who.int/publications/i/item/9789240045064.

(64) Khan, K.; Wasserman, G. A.; Liu, X.; Ahmed, E.; Parvez, F.; Slavkovich, V.; Levy, D.; Mey, J.; van Geen, A.; Graziano, J. H.; Factor-Litvak, P. Manganese Exposure from Drinking Water and Children's Academic Achievement. *NeuroToxicology* **2012**, *33* (1), 91−97.

(65) Wasserman, G. A.; Liu, X.; Parvez, F.; Factor-Litvak, P.; Ahsan, H.; Levy, D.; Kline, J.; van Geen, A.; Mey, J.; Slavkovich, V.; Siddique, A. B.; Islam, T.; Graziano, J. H. Arsenic and Manganese Exposure and Children's Intellectual Function. *NeuroToxicology* **2011**, *32* (4), 450−457.

(66) Oulhote, Y.; Mergler, D.; Barbeau, B.; Bellinger, D. C.; Bouffard, T.; Brodeur, M.-È.; Saint-Amour, D.; Legrand, M.; Sauvé, S.; Bouchard, M. F. Neurobehavioral Function in School-Age Children Exposed to Manganese in Drinking Water. *Environ. Health Perspect.* **2014**, *122* (12), 1343−1350.

(67) Post, J. E. Manganese Oxide Minerals: Crystal Structures and Economic and Environmental Significance. *Proc. Natl. Acad. Sci. U.S.A.* **1999**, *96* (7), 3447−3454.

(68) McClain, C. N.; Fendorf, S.; Webb, S. M.; Maher, K. Quantifying Cr(VI) Production and Export from Serpentine Soil of the California Coast Range. *Environ. Sci. Technol.* **2017**, *51* (1), 141−149.

(69) Hausladen, D. M.; Peña, J. Organic Buffers Act as Reductants of Abiotic and Biogenic Manganese Oxides. *Sci. Rep.* **2023**, *13* (1), 6498.

(70) Kim, J. G.; Dixon, J. B.; Chusuei, C. C.; Deng, Y. Oxidation of Chromium(III) to (VI) by Manganese Oxides Contribution from Texas Agriculture Experimental Station, Texas A&M University, College Station, TX. *Soil Science Society of America Journal* **2002**, *66* (1), 306−315.

(71) Wielinga, B.; Mizuba, M. M.; Hansel, C. M.; Fendorf, S. Iron Promoted Reduction of Chromate by Dissimilatory Iron-Reducing Bacteria. *Environ. Sci. Technol.* **2001**, *35* (3), 522−527.

(72) Papassiopi, N.; Vaxevanidou, K.; Christou, C.; Karagianni, E.; Antipas, G. S. E. Synthesis, Characterization and Stability of Cr(III) and Fe(III) Hydroxides. *Journal of Hazardous Materials* **2014**, *264*, 490−497.

(73) Rajapaksha, A. U.; Vithanage, M.; Ok, Y. S.; Oze, C. Cr(VI) Formation Related to Cr(III)-Muscovite and Birnessite Interactions in Ultramafic Environments. *Environ. Sci. Technol.* **2013**, *47* (17), 9722−9729.

(74) McClain, C. N.; Fendorf, S.; Johnson, S. T.; Menendez, A.; Maher, K. Lithologic and Redox Controls on Hexavalent Chromium in Vadose Zone Sediments of California's Central Valley. *Geochim. Cosmochim. Acta* **2019**, *265*, 478−494.

(75) Hausladen, D. M.; Alexander-Ozinskas, A.; McClain, C.; Fendorf, S. Hexavalent Chromium Sources and Distribution in California Groundwater. *Environ. Sci. Technol.* **2018**, *52* (15), 8242−8251.